Electronic Supplementary Material (ESI) for Energy & Environmental Science.

Supplementary Information

Tailored oxide interface creates dense Pt single-atom catalysts with high catalytic activity

Mi Yoo[1‡], Young-Sang Yu[2‡], Hyunwoo Ha[1‡], Siwon Lee[3‡], Jin-Seok Choi[4], Sunyoung Oh[5,6],
Eunji Kang[1], Hyuk Choi[1], Hyesung An[1], Kug-Seung Lee[7], Jeong Young Park[5,6],
Richard Celestre[2], Matthew A. Marcus[2], Kasra Nowrouzi[2], Doug Taube[2], David A. Shapiro[2],
WooChul Jung[3*], Chunjoong Kim[1*], and Hyun You Kim[1*]

[1]Department of Materials Science and Engineering, Chungnam National University,
Daejeon 34134, Republic of Korea

[2]Advanced Light Source, Lawrence Berkeley National Laboratory, Berkeley, California
94720, United States of America

[3]Department of Materials Science and Engineering,
Korea Advanced Institute of Science and Technology (KAIST),
Daejeon 34141, Republic of Korea

[4]KAIST Analysis Center for Research Advancement,
Korea Advanced Institute of Science and Technology (KAIST),
Daejeon 34141, Republic of Korea

[5]Center for Nanomaterials and Chemical Reactions, Institute for Basic Science (IBS),
Daejeon 34141, Republic of Korea

[6]Department of Chemistry, Korea Advanced Institute of Science and Technology (KAIST),
Daejeon 34141, Republic of Korea

[7]Pohang Accelerator Laboratory, Pohang University of Science and Technology,
Pohang 37673, Republic of Korea

‡These authors contributed equally to this work

[*]Corresponding authors. Email: wcjung@kaist.ac.kr (W.J.); ckim@cnu.ac.kr (C.K.); kimhy@cnu.ac.kr (H.Y.K.)

Contents

1. Methods

2. Supplementary Figures and Tables

3. Supplementary discussion

4. Full reference list for Fig. 5c

5. References

1. Methods

Synthesis of CeO_x-TiO_2 supporting oxide and *n*PT and *n*PCT catalysts

To synthesize CeO_x-TiO_2 hybrid-oxides and *n*PT and *n*PCT catalysts, titanium (IV) oxide (anatase, #45603, Alfa Aesar) powder, cerium (III) nitrate hexahydrate ($CeN_3O_9{\cdot}6H_2O$, #11330, Alfa Aesar) powder, and chloroplatinic acid (H_2PtCl_8 8 wt.% in H_2O, Sigma-Aldrich) solution were used. As-received anatase-TiO_2 powders were heat-treated under air at 500 °C for 4 hours before use. CeO_x-TiO_2 oxide supports were synthesized by the wet impregnation method. Initially, 1 g of TiO_2 powder and varying contents of Ce precursor were dispersed in 60 ml of deionized (DI) water and stirred for 2 hours at 70 °C. The initial amount of Ce was set to 1 wt.% with respect to the calculated amount of Ti ions in the TiO_2 powder. The solution was dried at 110 °C for 12 hours and calcined in air at 500 °C for 8 hours with a heating rate of 2 $°C{\cdot}min^{-1}$. To synthesize *n*PCT and *n*PT catalysts, varying amounts of H_2PtCl_8 solution was added to 60 mL of deionized water with 1 g of CeO_x-TiO_2 or TiO_2 powder. The initial amount of Pt was set to 0.25, 0.5, and 1.0 wt.% with respect to the total weight of *n*PCT or *n*PT catalysts. After Pt impregnation, the resulting samples were dried at 110 °C for 12 hours and calcined in air at 500 °C for 3 hours to remove the residual chlorine.

Post-experimental analysis

The Pt recovery ratio of the *n*PT and *n*PCT catalysts was estimated by an inductively coupled plasma atomic emission spectrometer (ICP-AES, Perkin-Elmer OPTIMA 7300 DV; see Table S1). The real averaged Pt wt.% values were used for estimation of the electrochemical surface areas (ECSAs) of *n*PT and *n*PCT catalysts and their MA for CO oxidation.

High-resolution transmission electron microscopy (HRTEM) analysis was conducted to identify the morphology of Pt nanoparticles dispersed on TiO_2 and CeO_x-TiO_2 supports with a Tecnai G^2 F30 S-TWIN TEM (FEI) operated at an accelerating voltage of 300 kV. For microstructural analysis of the *n*PCT system, high-angle annular dark-field (HAADF) scanning transmission electron microscopy (STEM) analysis was performed using a Titan Double CS-corrected TEM (Titan cubed G2 60-300, FEI) operated at accelerating voltages ranging from 60 to 300 kV. The compositions of the catalysts were analyzed using an energy-dispersive X-ray spectroscopy (EDS) detector. *Ex-situ* X-ray absorption spectroscopy (XAS) analysis was performed on the catalysts across the Pt L_3-edge using the 8C beamline at Pohang Accelerator Laboratory (PAL) with a Si (111) double-crystal monochromator. The raw spectra of all samples were energy-calibrated with a Pt foil in front of the third ion chamber simultaneously, and the spectra were acquired in fluorescence mode using a gas ionizing detector at room temperature. The raw data was fitted using the PyMca and SIXPACK programs. Detailed structural refinement using XAFS was not studied in this work due to complexity of the structure in the nanoscale. XANES spectra were fitted by a linear combination using reference standard spectra of Pt and PtO_2 to provide quantitative information about degree of oxidation of Pt among the catalysts (Table S2)[1]. Meanwhile, fitting of EXAFS and XANES spectra using the calculated spectra of intermediate phases such as PtO, Pt_2O_3, Pt_3O_4, etc. was not considered for the clarity in the interpretation though those phases can be present in *n*PT and *n*PCT catalysts[2].

The ECSAs of two different metal-oxide-supported Pt catalysts were evaluated by CO stripping tests[3]. All electrochemical measurements were conducted in a standard three-compartment electrochemical cell using a glassy carbon rotating disk electrode (RDE), Pt wire, and a saturated calomel electrode (SCE) as the working, counter, and reference electrodes, respectively. All measurements were performed at 20 °C in 0.1 M $HClO_4$. The catalyst ink slurry was prepared by mixing each catalyst with 20 μL of DI water, 54.7 μL of 5 wt.% Nafion solution as a binding material, and 630 μL of 2-propanol. Following mixing and ultrasonication, a drop of the ink slurry was loaded onto a glassy carbon substrate (geometric surface area of 0.196 cm^2). The dried electrode was then transferred to the electrochemical cell. CO was adsorbed on prepared *n*PCT and *n*PT catalysts at 0.05 V during the introduction of 100% CO gas for 20 min. The electrolyte was purged by Ar gas for 25 min after full coverage of CO_{ad} on the catalyst surfaces, and then CO_{ad} was oxidized by a potential sweep between 0.05 and 1.05 V with a scan rate of 20 $mV \cdot s^{-1}$. During CO stripping, CO is desorbed from the electrocatalyst surface. The value is then compared to evaluate the surface area by assuming the desorption value for a monolayer of CO (420 $C \cdot cm^{-2}$)[4].

Chemical mapping by soft X-ray scanning transmission X-ray microscopy (STXM)

Two-dimensional chemical composition maps were obtained using STXM combined with X-ray absorption spectroscopy (XAS) at the elliptically polarizing undulator beamline (7.0.1.2) at the Advanced Light Source (ALS), Lawrence Berkeley National Laboratory, Berkeley, CA (USA)[5]. A monochromatic X-ray beam is focused onto the catalytic particles by a 40 nm outer-zone-width Fresnel zone plate (FZP). An order-sorting aperture (OSA) blocks higher-order diffraction. Two-dimensional raster scans of the transmitted X-ray are recorded by an X-ray sensitive diode (Fig. S4). To ensure transparency of samples in soft X-ray region, the active catalytic particles were dispersed with an appropriate solvent onto a 50-nm-thick SiN_x window based micro-heater and sealed by a 50-nm-thick SiN_x top-cover (Hummingbird Scientific 1450 series, Fig. S4). Image spectra (i.e. repeated images at different energies) across the Ti *L*-edge and Ce *M*-edge allows us to have spectral sensitivity, with the finest energy step of 0.25 eV near the absorption resonance features (Fig. S5), from very small spots (~ 50 nm). The dwell times/pixel (0.1-2 msec) and slit sizes were chosen in consideration of the required spectral resolution and radiation stability (Fig, S6).

Operando liquid/gas flow nanoreactor

The catalytic particles were sealed in a microfluidic heating cell (Hummingbird Scientific 1450 series, Fig. S4) designed for liquid TEM[6, 7]. The microfluidic heating cell consists 50-nm-thick SiN_x membrane sandwich separated by a spacer with thickness of 500 nm gap for liquid/gas flow. The temperature of the micro-heater was controlled *via* the temperature-dependent resistivity with a closed-loop control. The resistivity versus temperature dependency of the heater was calibrated by the manufacturer (Hummingbird Scientific) on each batch of fabricated chips. Chloroplatinic acid (H_2PtCl_8 8 wt.% in H_2O) solution or a blend of Ar with 7% CO flowed through a 50 cm long polyether ether ketone (PEEK) tube with flow rates of 3 $\mu L \cdot min^{-1}$ and 1.5 sccm, respectively. Since the pressure difference between the STXM environment (lower than 10^{-6} Torr) and the nanoreactor interior causes the SiN_x window to bulge, the concave line profile of the transmitted X-ray intensity confirms the presence of liquid inside the nanoreactor (Fig. S4). Liquid injection time is estimated by the total volume of flowing channel versus flow rate and considered as the error range in the reaction time (Fig. 3).

Radiation dose estimation

Quantifying the radiation dose to ceria (CeO_2) is an important issue as the oxidation states can, in principle, be altered by prolonged X-ray irradiation[8]. The damage induced X-ray exposure leads to changes in the CeO_2 spectral shapes that are consistent with reduced Ce^{3+}[9]. The maximum allowed dose without structural and chemical changes was verified by the preliminary dose test with similar environments (i.e. the catalytic particles were sealed with 3 $\mu L \cdot min^{-1}$ H_2O flow in the identical nanoreactor) to *operando* STXM measurements (Fig. S6). The maximum aggregate dose used in the *operando* imaging experiments was limited within the stable dose range of the catalytic particle (Fig. S6). The X-ray flux incident on the sample was ~ 1 × 10^8 photons·s^{-1}. The dwell time for each pixel was typically 1 ms, so the dose for each pixel is ~ 1 × 10^5 photons·pixel^{-1}, which is 1.4 × 10^{-11} J·pixel^{-1} at 900 eV. The radiation dose is determined by $D = \mu N_0 h\nu \cdot \rho^{-1}$, where N_0 is the number of incident photons per unit area, $h\nu$ is the photon energy, ρ = 4.41 g·cm^{-3} is the mass density of CeO_x-TiO_2 nanostructures with 6 wt.% Ce addition and μ^{-1} is the attenuation length[10]. The dose per STXM image is calculated to be ~ 6.6 × 10^6 Gy. Note that the amount of Pt SAs is a negligible quantity in the dose calculations. In the range of the maximum allowed dose (more than 10 image spectra, Fig. S6), typical X-ray induced reduction effects were not observed.

Image processing

To eliminate image-to-image wobble with sub-pixel precision, the geometric transformation matrix (translation) between sequential STXM images was calculated by the intensity-based image registration (MathWorks, MATLAB R2019a) and applied to each image with bilinear interpolation. The STXM images (2 dimensional transmitted intensity, I) were converted to the absorbance image spectra (optical density, OD) by taking the log ratio of the incident (I_0) and transmitted (I) intensities in each pixel. In the averaged STXM image across the energy range, the pixels of which transmitted intensity are higher than 85 % of the brightest pixel were considered as a sample-free region for estimating I_0. To enhance the signal-to-noise ratio, the image spectra were filtered by local-means. The quantitative distributions of distinct chemical phases were mapped by analyzing the image spectra on a pixel-by-pixel basis with reference spectra (Fig. S7). A single pixel spectrum from the sample containing noninteracting chemical compounds is the linear superposition of the spectra of the single chemical compounds. The relative amounts of each component were calculated by applying a singular value decomposition method. The quality of each linear-combination fit was checked with the R-factor defined as, $R = \sum(\text{data - fit})^2 / \sum(\text{data})^2$. Pixels showing poor signal-to-noise ratios were filtered out by a lower bound of the R-factor (0.2).

Experimental catalyst performance test

The catalytic activities of CeO_x-TiO_2 powders and nPT and nPCT catalysts toward CO oxidation were measured in a fixed-bed quartz flow microreactor with an internal diameter of 4 mm. For all the measurements, we used 50 mg of catalyst mixed with 100 mg of quartz sand

and loaded between two plugs of quartz wool to prevent displacement of the catalyst. The reaction gas consisted of 1 vol% CO, 4 vol% O_2, and 95 vol% Ar and was fed at 50 mL·min^{-1}, corresponding to a weight hourly space velocity (WHSV) of 60,000 mL·g^{-1}·h^{-1}. The reactant and product gases were monitored in real time with a quadrupole mass spectrometer (QMS, PFEIFFER Vacuum GSD320) connected to the reactor outlet. The light-off curve was measured with a ramping rate at 3 °C·min^{-1}, after activating the catalysts in the reaction atmosphere up to 300 °C. The CO conversion ratio (%) was defined as 100 × (mol $CO_{,\,in}$ – mol $CO_{,\,out}$)/mol $CO_{,\,in}$. The signal of CO was corrected for the contribution from the cracking fragment of CO_2 with mass concentration determination mode.

CO-temperature programmed reduction (CO-TPR) tests were performed in a fixed-bed quartz flow microreactor. 0.25PT and 0.25PCT catalysts were pretreated at 100 °C for an hour under Ar 100 vol%. We used 100 mg of catalyst mixed with 200 mg of quartz sand and loaded between two plugs of quartz wool. The reaction gas consisted of 1 vol% CO and 99 vol.% Ar and was fed at 100 mL·min^{-1}, corresponding to a weight hourly space velocity (WHSV) of 60,000 mL·g^{-1}·h^{-1}. A ramping rate of 1 °C·min^{-1} applied from 50 °C to 200 °C and the catalyst was maintained at 200 °C for 4 hours. The reactant and product gases were monitored in real time with a quadrupole mass spectrometer (QMS, PFEIFFER Vacuum GSD320) connected to the reactor outlet. The CO_2 concentration in the outlet gas was measured *in-situ*.

***In-situ* Infrared (IR) Spectroscopy**

Diffuse reflectance infrared Fourier transform spectroscopy (DRIFTS) measurements were performed on an Agilent Cary 660 spectrometer equipped with a high-temperature reaction chamber (Harrick) with a ZnSe window and a mercury cadmium telluride (MCT) detector. Additionally, the IR reactor chamber was connected to a quadrupole mass spectrometer (QMS) for gas analysis. All samples were pressed with a stainless steel mesh to make a pellet, preventing contamination of the reaction cell. The catalysts were loaded into the reaction chamber and reduced *in-situ* at 250 °C in 5% H_2/He (100 mL·min^{-1}) for 1 hour, followed by purging the reactor for 30-60 min with He gas at 25 °C. Next, all the catalysts were exposed to 1% CO and 4% O_2 balanced with the He gas (100 mL·min^{-1}) by using mass flow controllers (BROOKS instrument). For the CO oxidation reaction, the reaction temperature was increased from 25 °C to 300 °C with a ramp rate of 5 °C·min^{-1}. The IR reactor chamber is connected to a heater to vary the temperature. Each spectrum was recorded using 32 scans at a

4 cm^{-1} resolution. All of the spectral results were transformed using the Kubelka–Munk function.

Density functional theory calculations

We performed GGA-level spin-polarized density functional theory (DFT) calculations with the VASP code[11, 12] and the PW91 functional[13]. The Ti *d*-orbitals and Ce *f*-orbitals were treated with the DFT+U method with U_{eff} = 4.5 eV applied for Ti and Ce ions[14]. The reliability of the U_{eff} value was experimentally verified by the XPS/UPS spectra of CeO_x supported on the rutile TiO_2 (110) system[15] and was confirmed in our previous study[16]. The interaction between the ionic core and the valence electrons was described by the projector augmented wave method[17], and the valence electrons were treated with a plane wave basis up to an energy cutoff of 400 eV. The Brillouin zone was sampled at the Γ-point. The convergence criteria for the electronic structure and the geometry were 10^{-4} eV and 0.03 $eV \cdot Å^{-1}$, respectively. We used the Gaussian smearing method with a finite temperature width of 0.05 eV improve convergence of states near the Fermi level.

A diagonal (surface vectors of [1 -1 -1] and [0 1 0]) 3×4 slab model with three layers of TiO_2 was used to model the TiO_2(101) surface. A CeO_2 cluster was deposited on TiO_2(101) to describe the morphology of the CeO_x-TiO_2 interface. Details of the thermodynamic interpretation of CeO_x-TiO_2 hybrid-oxide formation can be found elsewhere[16].

2. Supplementary Figures and Tables

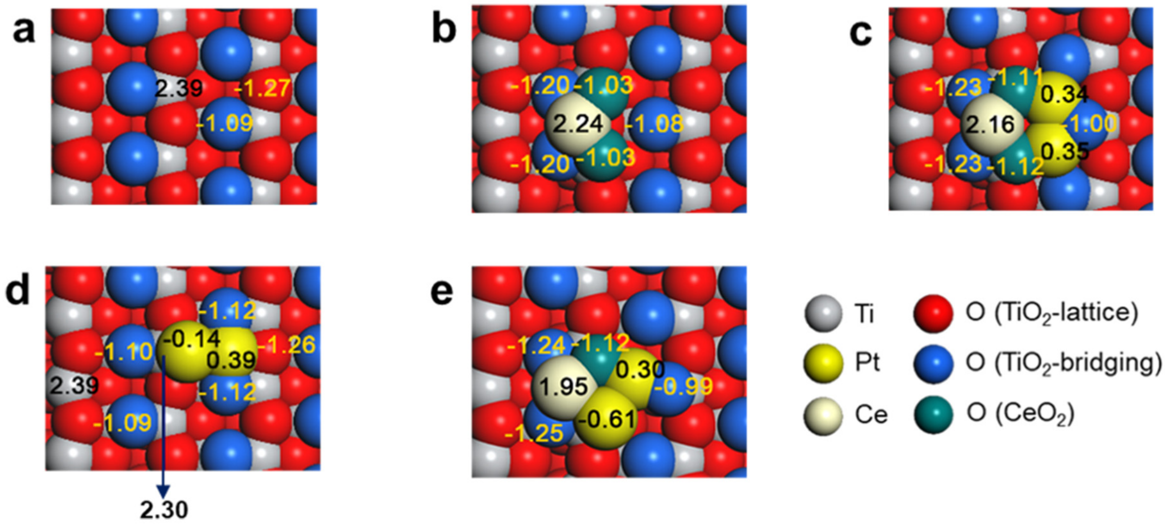

Figure S1. Electronic interaction between composing elements of Pt/TiO$_2$ (PT) and Pt/CeO$_x$-TiO$_2$ (PCT) model catalysts. **a-e**, Bader charge analysis of (**a**) TiO$_2$(101), (**b**) CeO$_2$-TiO$_2$(101), (**c**) Pt$_2$/CeO$_2$-TiO$_2$(101), and (**d**) Pt$_2$/TiO$_2$(101), (**e**) Pt$_2$/CeO-TiO$_2$(101). Black and yellow numbers represent the Bader charge of metal ions and oxygen ions, respectively. A Pt$_2$ cluster donates electrons to supporting oxides. The Pt$_2$ at the CeO$_x$-TiO$_2$ interface donates more electrons than the cluster on TiO$_2$(101), reducing the adjacent Ce ion. Decreased Bader charge number of the Ce ion in (**c**) from that in (**e**) shows that the Ce ion was further reduced upon oxygen vacancy formation.

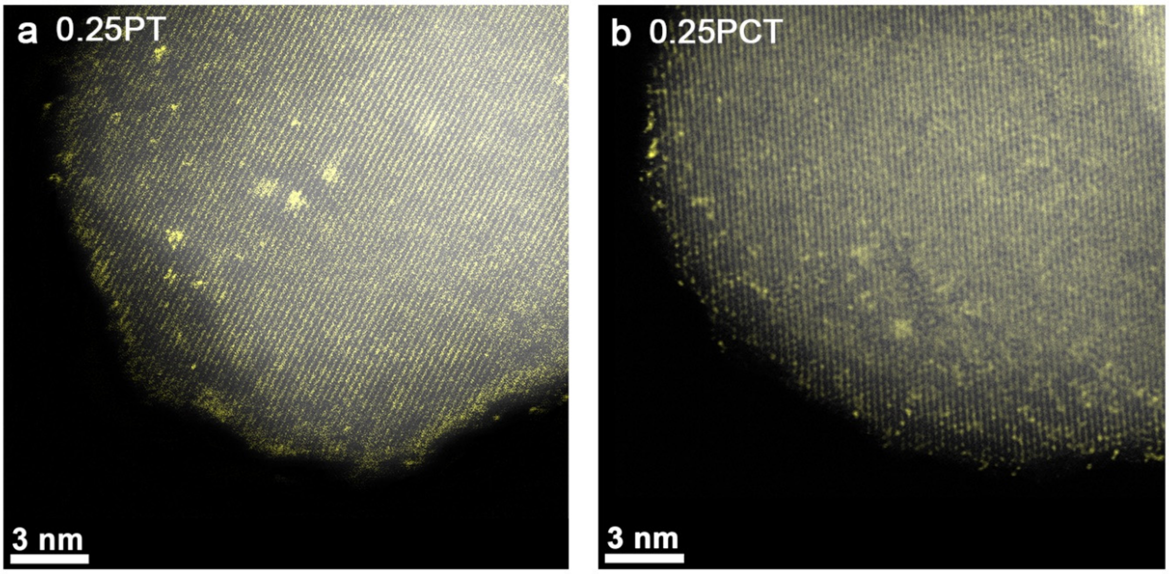

Figure S2. **Additional HAADF-STEM images of the studied catalysts.** **a**, 0.25PT, **b**, 0.25PCT.

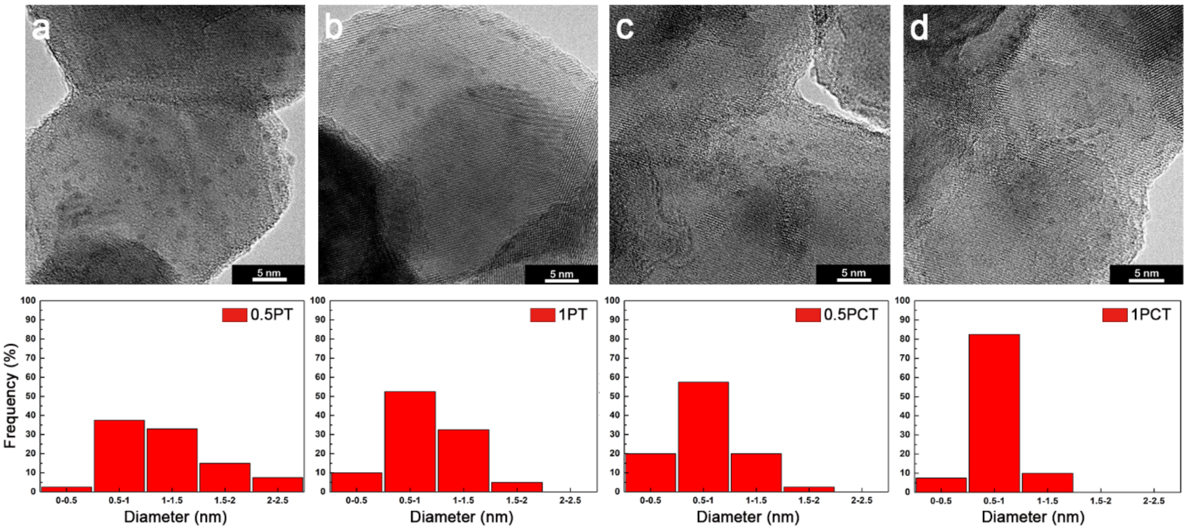

Figure S3. TEM images of *n*PT and *n*PCT catalysts and the size distribution of Pt clusters and nanoparticles. a, 0.5PT and **b**, 1.0PT catalysts. **c,** 0.5PCT and **d**, 1.0PCT catalysts.

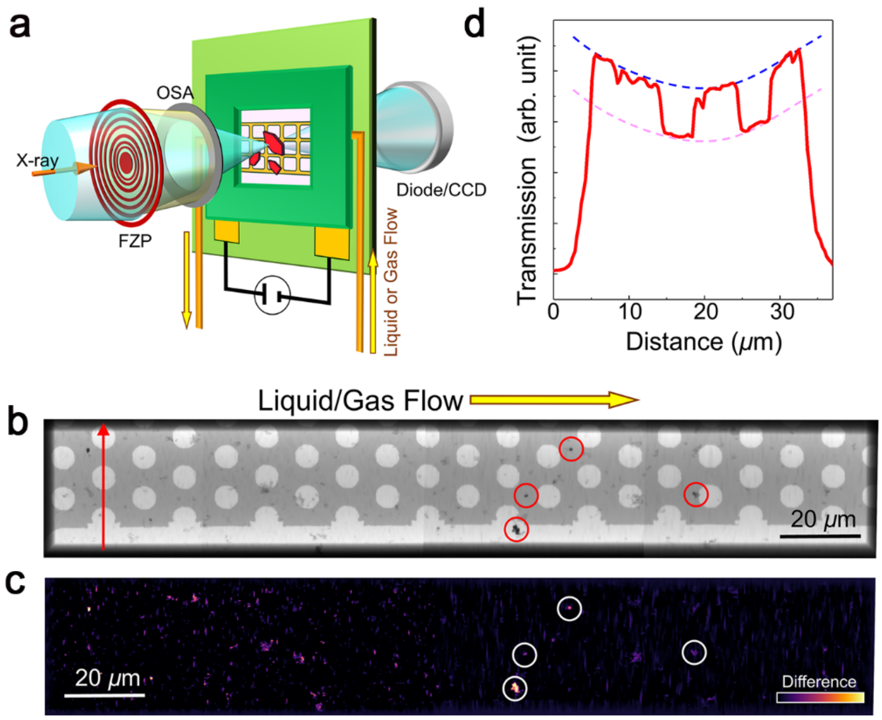

Figure S4. *Operando* synchrotron-based soft X-ray scanning transmission X-ray microscopy (STXM) combined with the liquid flow nanoreactor. a, Diagram of *operando* liquid/gas flow nanoreactor for STXM. Active catalytic particles with a micro-heater are sealed by a 50-nm-thick SiN_x window sandwich. **b**, Representative STXM image of the nanoreactor. **c**, Identifications of active catalytic particles. Optical density difference map between 879 eV (pre-edge) and 884 eV (near Ce M_5 absorption edge) gives a contrast only at the active catalytic particle sites (solid red and white circles in (**b**) and (**c**), respectively). **d**, Line profile (dotted blue line, a guide to eye) of STXM image across the nanoreactor along solid red line in (**b**).

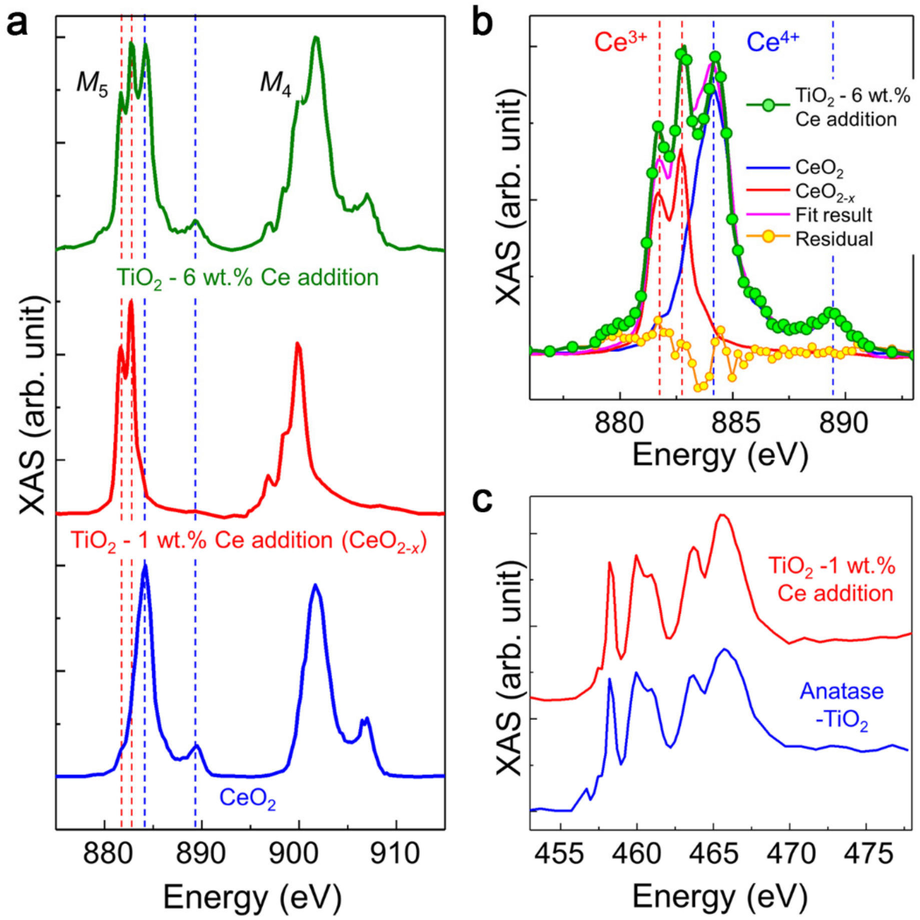

Figure S5. X-ray absorption near edge structure (XANES). a, Cerium *M*-edge XANES of CeO_x-TiO_2 nanostructures with respect to the amount of Ce-loading. Reference spectra (solid blue line) taken for commercial CeO_2 powder (#202975, Aldrich) are also shown for comparison. Energy positions of M_5-edge absorption features for Ce^{3+} and Ce^{4+} are indicated as dotted red and blue lines, respectively. **b**, Zoomed cerium M_5-edge absorption spectra for CeO_x-TiO_2 nanostructures with 6 wt.% Ce addition (solid green line with filled circles). Simulated spectra (solid magenta line) is a result of a linear combination fit with reference spectra from CeO_x-TiO_2 with 1 wt.% Ce addition (CeO_{2-x}, solid red line) and pure CeO_2 (solid blue line). The simulated concentration of CeO_2 is 56.01 %. The residual spectrum (solid orange line with scatters) is the difference between the experimental and the simulated spectrum. **c**, Titanium *L*-edge XAS of CeO_x-TiO_2 nanostructures with 1 wt.% Ce addition and Anatase-TiO_2[18, 19].

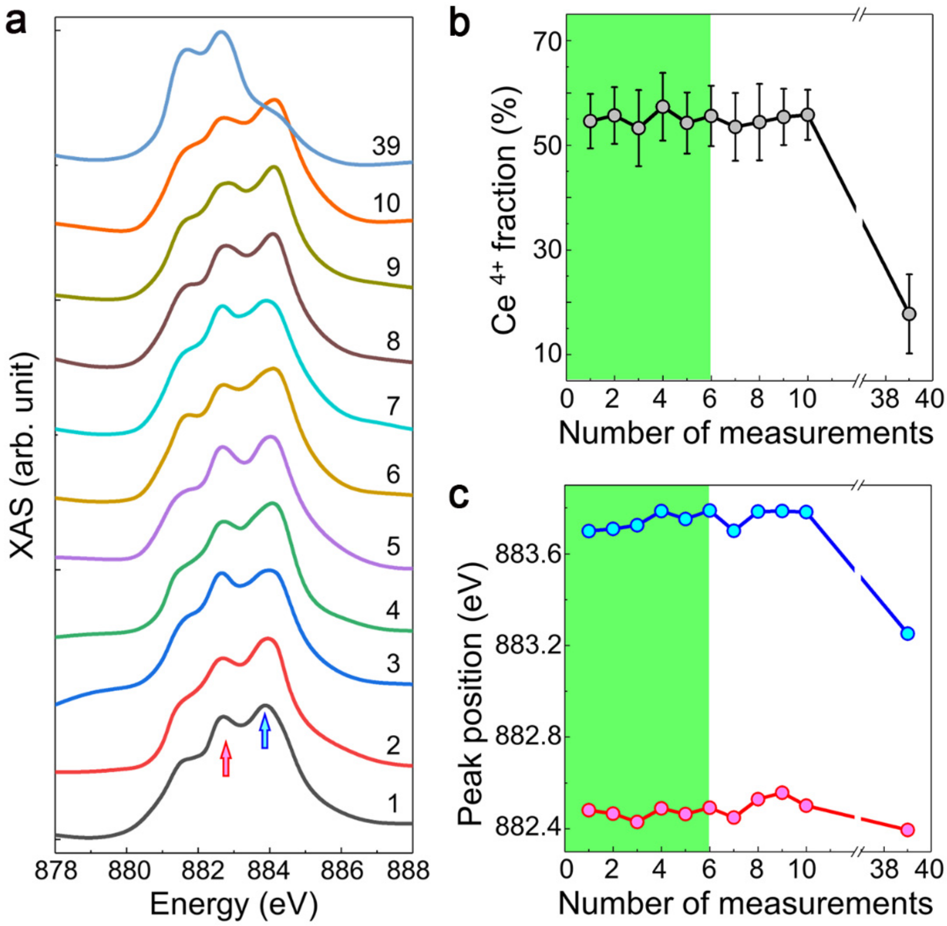

Figure S6. Stability of the catalytic particles under the X-ray beam dose. a, Averaged Cerium *M*-edge XANES of identical active catalytic particle site. The numbers indicate the number of stacks taken. **b**, Ce^{4+} fraction versus the number of measurements. Points and error bars indicate average and standard deviation of Ce^{4+} fraction from entire particle region, respectively. **c**, Energy positions of M_5-edge absorption features for Ce^{3+} [red arrow in (**a**), solid red line with scatters] and Ce^{4+} [blue arrow in (**a**), solid blue line with scatters]. The maximum aggregate dose used in our *operando* imaging experiments is limited within the stability dose of the catalytic particle [green shaded area in (**b**) and (**c**)].

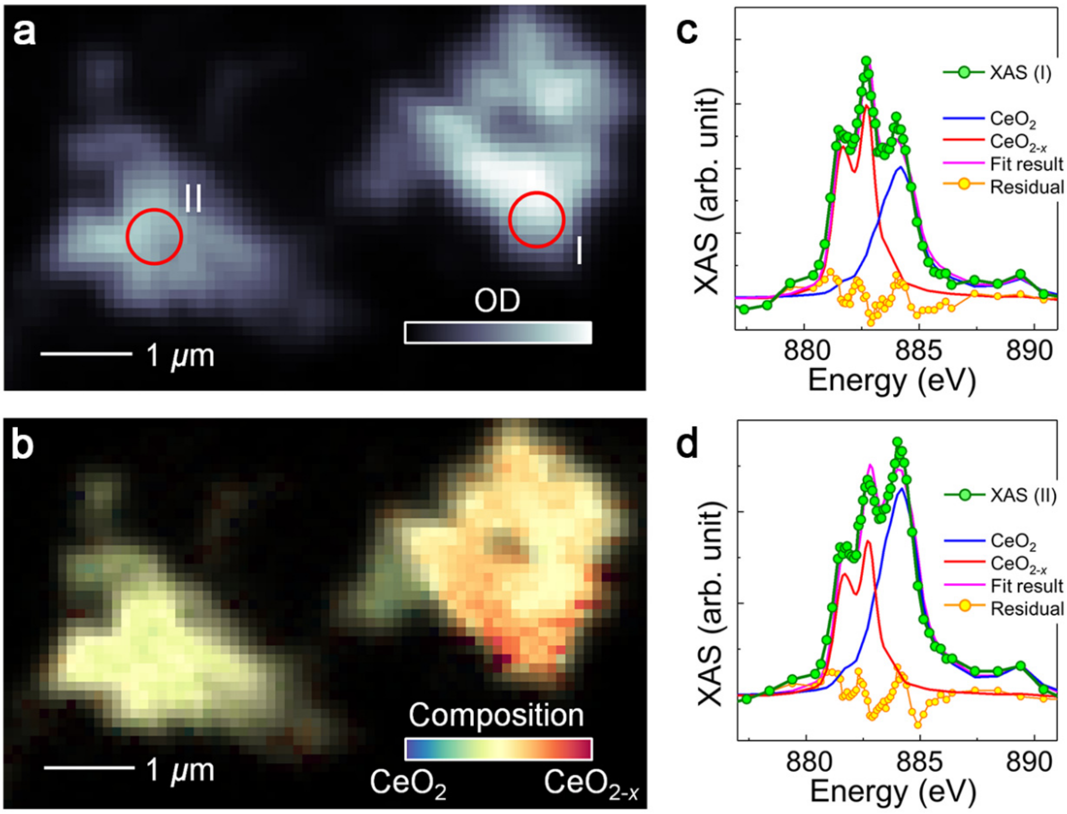

Figure S7. Chemical mapping of Ce oxidation states. a, Averaged optical density map across Ce M_5-edge. **b**, Chemical phase maps obtained by linear combination fits of XANES at each pixel. The fitting results (chemical information) and averaged optical density (morphological information) are presented by color legend and transparency, respectively. The presence of CeO_2 and CeO_{2-x} assigned colors blue and red, respectively. **c**, **d**, Representative XANES (solid green line with scatters) from highlighted areas I and II in (**a**) with reference spectra from CeO_x-TiO_2 with 1 wt.% Ce addition (CeO_{2-x}, solid red line) and pure CeO_2 (solid blue line). The concentrations of CeO_{2-x} for the regions I and II are 59.6 % and 42.9 %, respectively.

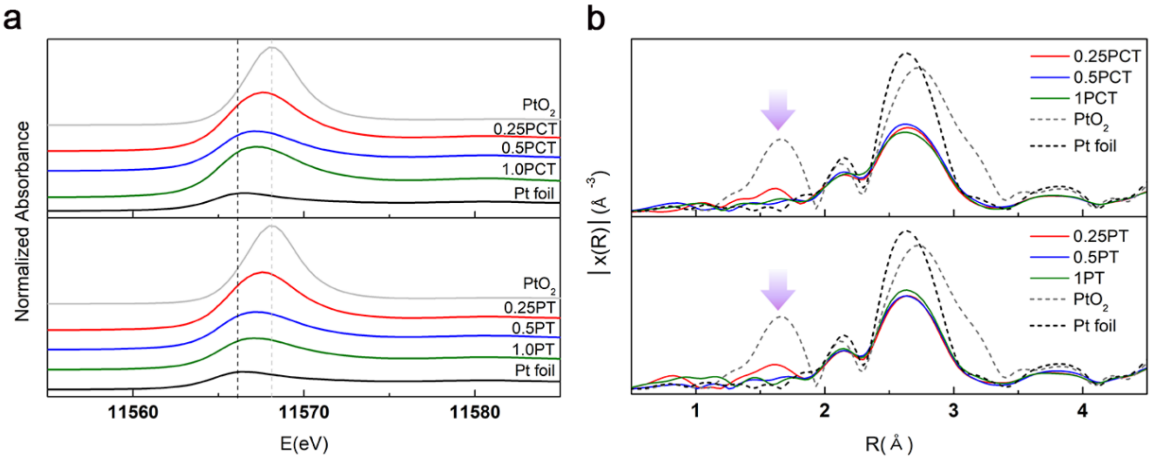

Figure S8. X-ray absorption spectra of *n*PCT and *n*PT catalysts. a, Normalized Pt L_3-edge XANES spectra of *n*PCT and *n*PT catalysts. **b**, EXAFS analysis result of *n*PCT and *n*PT catalysts.

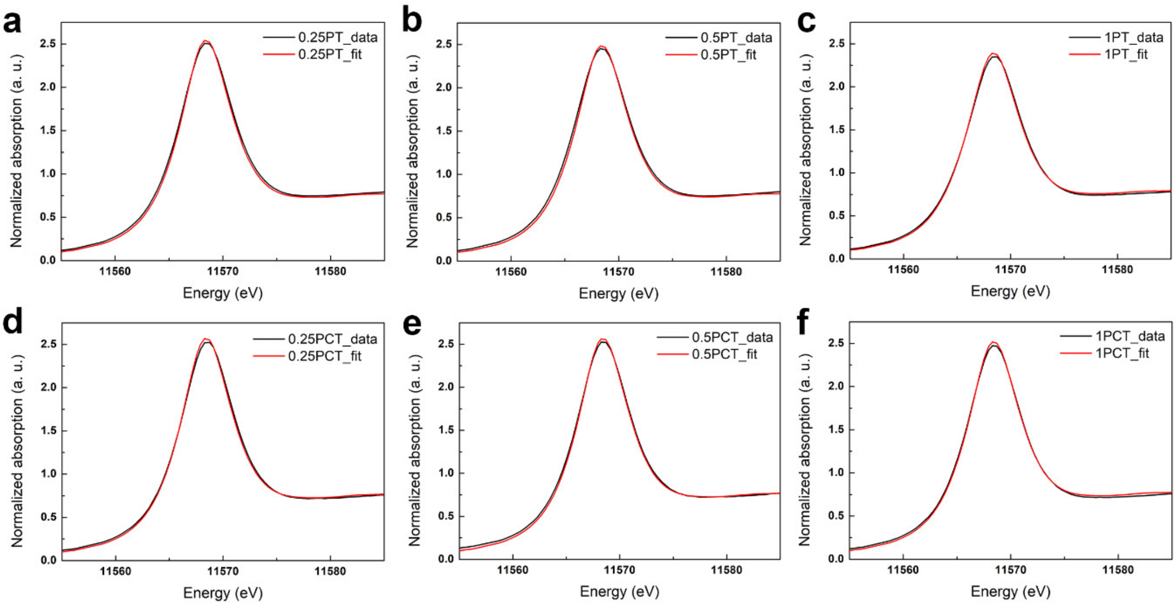

Figure S9. XANES linear fitting results. a-c, *n*PT. **d-f**, *n*PCT catalysts.

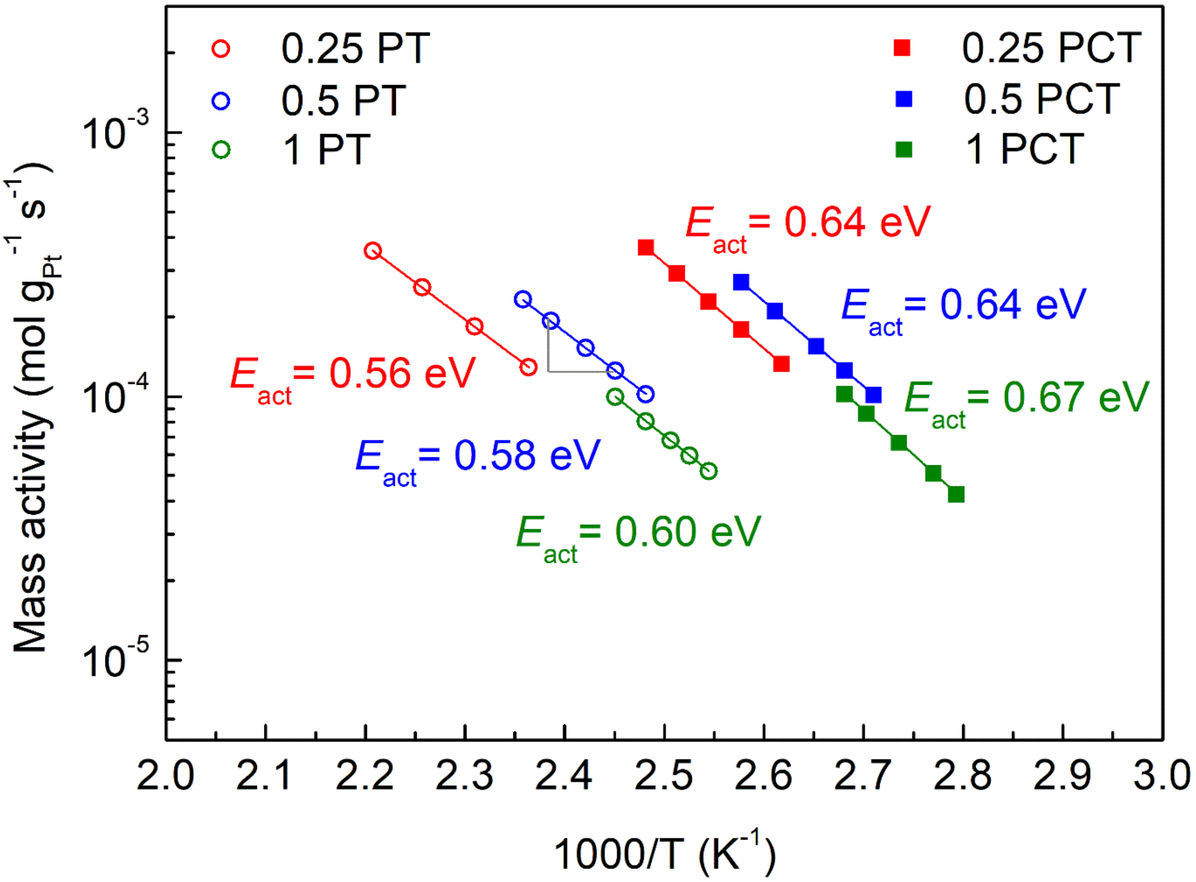

Figure S10. **Arrhenius plot of *n*PT and *n*PCT catalysts.**

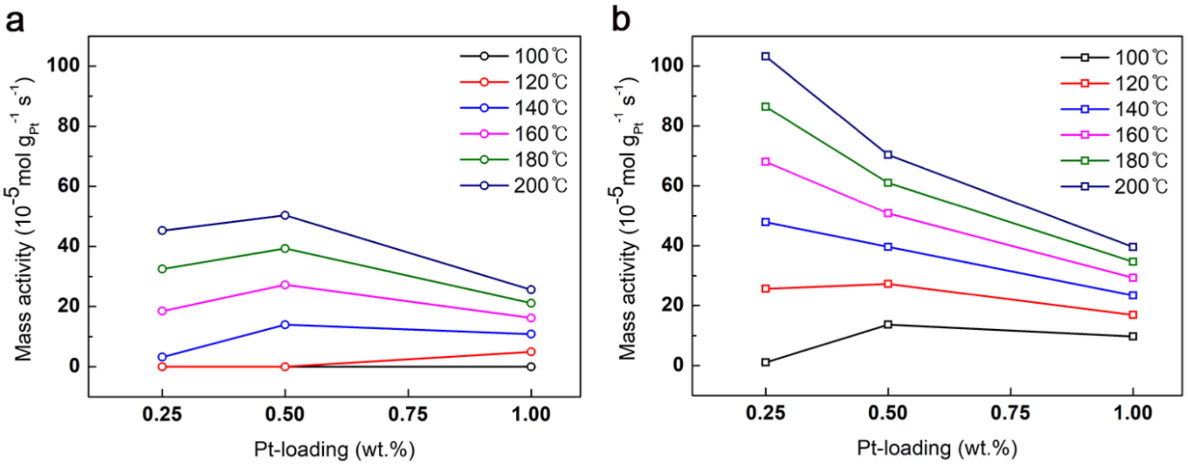

Figure S11. **Temperature dependent evolution of mass activity (MA) of studied catalysts.** **a**, *n*PT and **b**, *n*PCT.

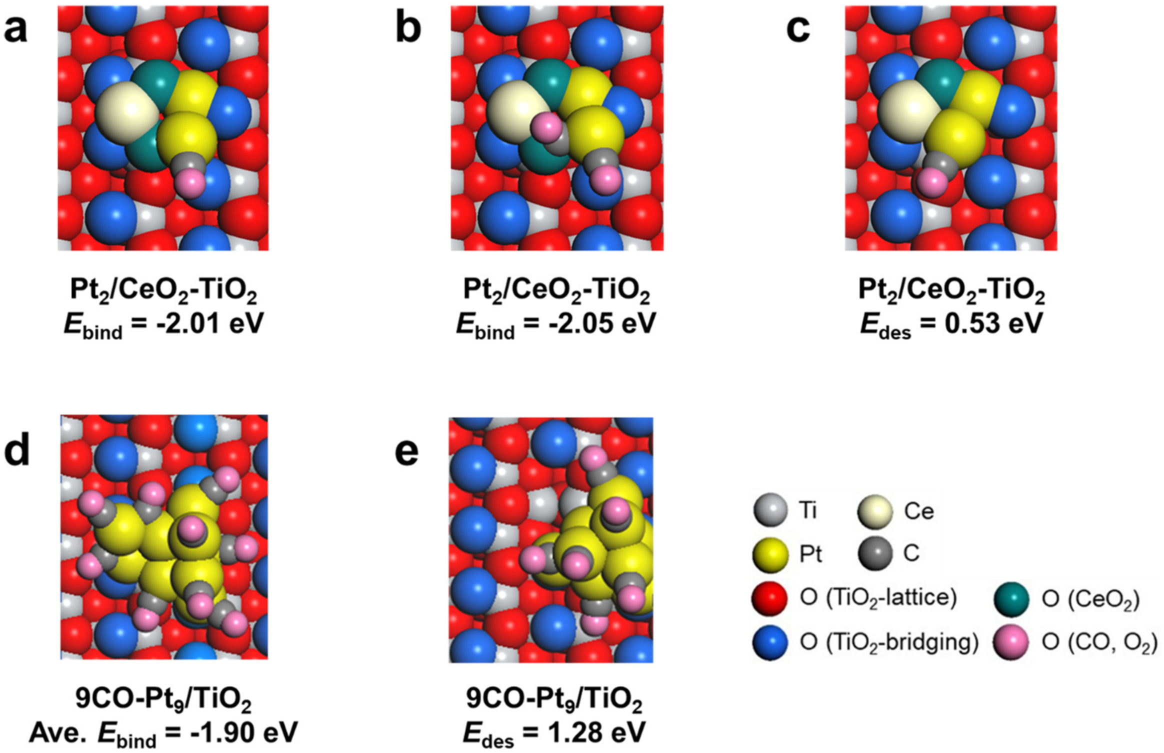

a: Pt_2/CeO_2-TiO_2, E_{bind} = -2.01 eV

b: Pt_2/CeO_2-TiO_2, E_{bind} = -2.05 eV

c: Pt_2/CeO_2-TiO_2, E_{des} = 0.53 eV

d: 9CO-Pt_9/TiO_2, Ave. E_{bind} = -1.90 eV

e: 9CO-Pt_9/TiO_2, E_{des} = 1.28 eV

Figure S12. **DFT-calculated CO binding and desorption energy values of Pt_2/CeO_x-TiO_2 and Pt_9/TiO_2. a, b**, The first and the second CO binding energies, E_{bind}, of Pt_2 cluster supported on CeO_x-TiO_2. **c**, Energy of CO production (desorption), E_{des}, from (**b**). **d**, Average E_{bind} of 9 CO molecules adsorbed on Pt_9/TiO_2. **e**, E_{des} of CO_2 from (**d**).

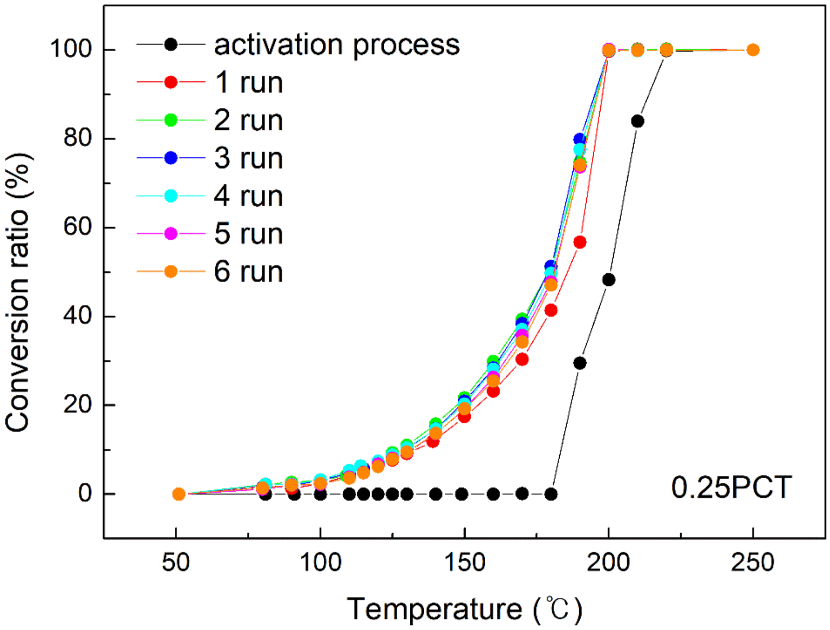

Figure S13. Light-off curves of 0.25PCT for repeating CO oxidation cycles. The E_{act} was converged to 0.64 eV above the 2nd cycle.

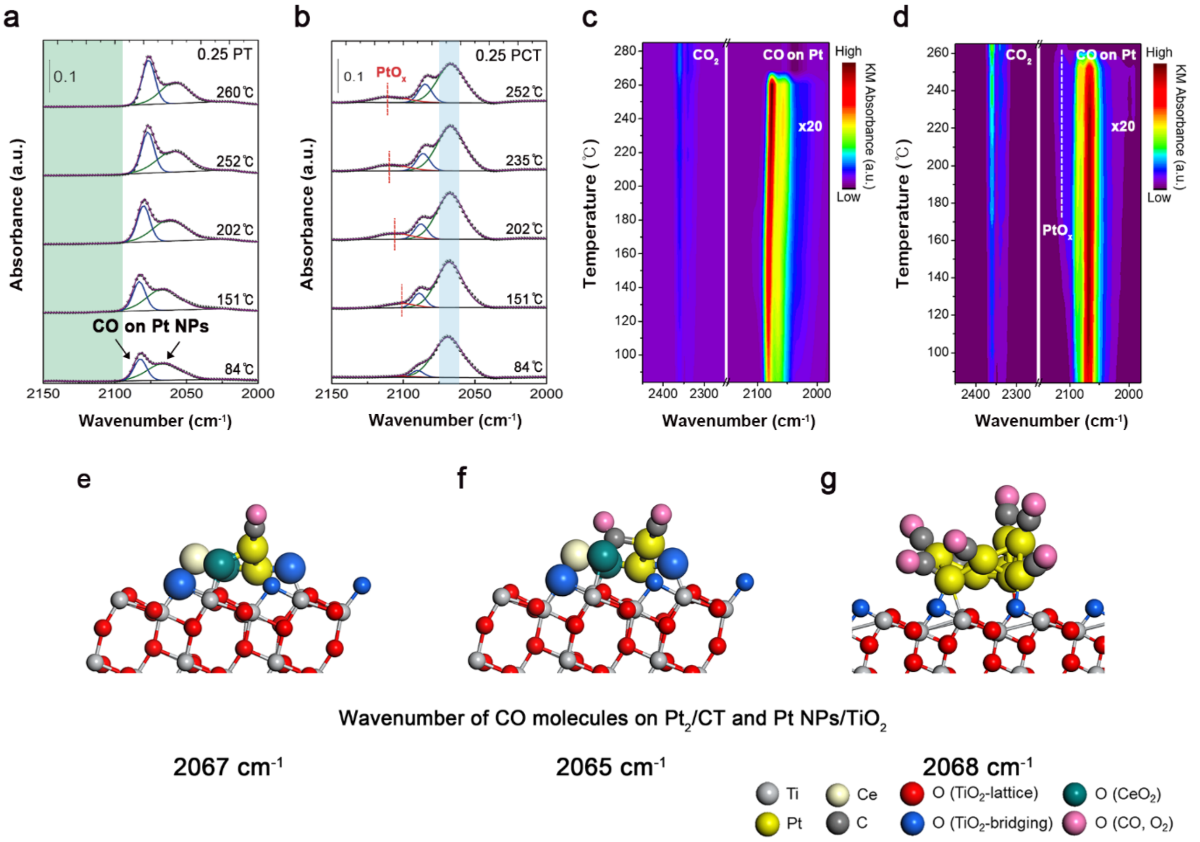

Figure S14. **a**, **b**, *In-situ* DRIFT spectra of 0.25PT and 0.25PCT. The green-highlighted area in (**a**) depicts a typical IR frequency range of Pt-SAs supported on TiO_2 and CeO_2. **c**, **d**, 2D color scale map of 0.25PT and 0.25PCT. **e-g**, DFT-calculated IR frequency of PCT- and PT-bound CO molecules. (**e**) Pt-bound single CO molecule of Pt_2/CeO_2-TiO_2. (**f**) Pt-bound two CO molecules of Pt_2/CeO_2-TiO_2. (**g**) Pt-bound multiple CO molecules of Pt_9/TiO_2. DFT calculated CO stretch frequency values in (**e**), (**f**), and (**g**) confirm that the CO molecules adsorbed on Pt-SAs of 0.25PCT attribute to the blue-highlighted emphasized spectra in (**b**).

Table S1. Pt concentration and recovery ratio determined by ICP-AES.

Catalysts	***n*PT**			***n*PCT**		
Targeted Pt-loading (wt.%)	0.25	0.5	1.0	0.25	0.5	1.0
Measured Pt-content (wt.%)	0.18	0.32	0.63	0.20	0.37	0.64

Table S2. XANES linear fitting results of *n*PT and *n*PCT catalysts

Catalyst	**Pt (%)**	**PtO_2 (%)**
0.25PCT	2.2	97.8
0.5PCT	2.6	97.4
1.0PCT	6.0	94.0
0.25PT	4.2	95.8
0.5PT	8.3	91.7
1.0PT	14.8	85.2

Table S3. Catalytic properties of *n*PT and *n*PCT catalysts for CO oxidation.

Catalysts	***n*PT**			***n*PCT**		
Pt-loading (wt.%)	0.25	0.5	1.0	0.25	0.5	1.0
T_{50} (°C)	204	191	170	178	143	135
T_{100} (°C)	220	194	175	200	170	155
Activation energy barrier (eV)[a]	0.56	0.58	0.60	0.64	0.64	0.67
Mass activity at 140 °C (10^{-5} mol/sec·g_{Pt})	3.17	13.97	10.85	47.87	39.62	23.39

[a] Estimated from the Arrhenius plot (**Fig. S10**)

3. Supplementary discussion

3.1 *Ex-situ* STXM analysis.

Since metal cations are intermixed at the oxide-oxide interface, leading to stabilization of the oxygen vacancy[20], the overall oxidation state of the CeO_x architectures depends on the ratio of Ce cation at the interface (largely Ce^{3+}) to the bulk region (Ce^{4+}). X-ray absorption near edge structure (XANES) at the Ce *M*-edge clearly shows a large fraction of the interfacial trivalent-Ce-cation. The overall Ce oxidation state varies with the amount of Ce loading (Fig. S5). Although the fraction of the trivalent-Ce-cations in the CeO_x-TiO_2 (1 wt.% Ce addition) was not easy to estimate quantitatively, its distinct spectral shape and relative energy positions of the absorption features compared with pure CeO_2 reference spectra clearly confirmed that the reduced phases (Ce^{3+}) is predominant in the CeO_x architectures with 1 wt.% Ce-loading (hereafter, CeO_{2-x}), while the remaining Ce cations are in the Ce^{4+} state[21]. As the amount of Ce-loading increases, the spectra increasingly resemble that of the bulk. Fig. S5b shows the XANES for the CeO_x-TiO_2 with 6 wt.% Ce addition superimposed on a model spectrum simulated by the linear-least-squares fitting method with CeO_2 and CeO_{2-x} spectra as the end members. Based on the compositional uncertainty of the CeO_{2-x}, the fraction of the tetravalent-Ce-cations is more than 56 % in the CeO_x architectures with 6 wt.% Ce-loading. The linear-least-squares fitting results from more than 800 XANES indicate an inter-particle heterogeneity (Fig. S7) with the quantitative fraction of the tetravalent-Ce-cations (average: 47 %, standard deviation: 10 %). In spite of the formation of trivalent-Ce-cations, identical Ti *L*-edge XANES showed the preservation of its anatase crystal structure and negligible change of Ti oxidation states (Fig. S5). Note that XANES detects the oxidation states of the entire CeO_x-TiO_2 nanoarchitectures (e.g. including surface, bulk, and ceria-titania interface) due to its transmission experimental geometry.

3.2 DRIFT-IR analysis of 0.25PT and 0.25PCT catalysts.

In-situ DRIFT IR analysis results collected under the CO oxidation condition (1% CO, 4% O_2, and He bal.) show that typical CO stretch frequencies of Pt-SAs supported on TiO_2[22, 23] or CeO_2[24] observed at around 2100 cm^{-1} are absent in 0.25PT, meaning that 0.25 wt.% of Pt-loading was relatively high to separately stabilize Pt-SAs on our TiO_2 powder (Fig. S14). The dual peaks centered at 2082 and 2065 cm^{-1} can be assigned to the linear CO molecules bound to the Pt clusters and nanoparticles[22, 23]. Although STEM images confirm that high density Pt-SAs were exclusively formed in 0.25PCT (Fig. S2b), the CO stretch frequency at around 2100 cm^{-1} was absent in 0.25PCT too (Fig. S14). Interestingly, we found that the DFT-calculated stretch frequencies of the CO molecules bound to the Pt_2 of Pt_2/CeO_x-TiO_2 were significantly red-shifted to 2067 cm^{-1} and 2065 cm^{-1}, confirming the experimental results: absent of the peaks at around 2100 cm^{-1} and emphasized IR peak centered at around 2065 cm^{-1} in 0.25PCT (Fig. S14).

4. Full reference list for Fig. 5c

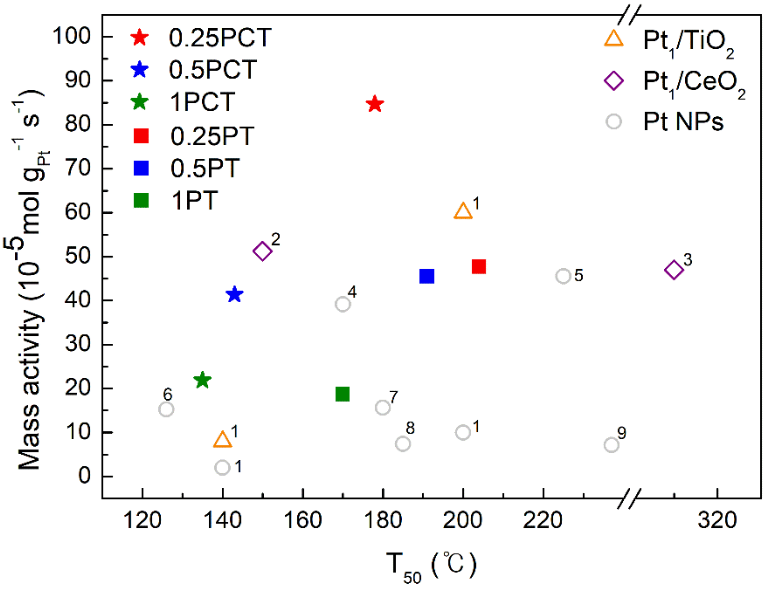

1. L. DeRita, S. Dai, K. Lopez-Zepeda, N. Pham, G. W. Graham, X. Pan and P. Christopher, *J. Am. Chem. Soc.*, 2017, **139**, 14150-14165.
2. C. Wang, X.-K. Gu, H. Yan, Y. Lin, J. Li, D. Liu, W.-X. Li and J. Lu, *ACS Catal.*, 2017, **7**, 887-891.
3. L. Nie, D. Mei, H. Xiong, B. Peng, Z. Ren, X. I. P. Hernandez, A. DeLaRiva, M. Wang, M. H. Engelhard, L. Kovarik, A. K. Datye and Y. Wang, *Science*, 2017, **358**, 1419.
4. A. M. Gänzler, M. Casapu, P. Vernoux, S. Loridant, F. J. Cadete Santos Aires, T. Epicier, B. Betz, R. Hoyer and J.-D. Grunwaldt, *Angew. Chem. Int. Ed.*, 2017, **56**, 13078-13082.
5. V. P. Santos, S. A. C. Carabineiro, P. B. Tavares, M. F. R. Pereira, J. J. M. Órfão and J. L. Figueiredo, *Appl. Catal. B: Environ.*, 2010, **99**, 198-205.
6. J. Chen, Y. Wanyan, J. Zeng, H. Fang, Z. Li, Y. Dong, R. Qin, C. Wu, D. Liu, M. Wang, Q. Kuang, Z. Xie and L. Zheng, *ACS Sus. Chem. Eng.*, 2018, **6**, 14054-14062.
7. S. Gatla, D. Aubert, V. Flaud, R. Grosjean, T. Lunkenbein, O. Mathon, S. Pascarelli and H. Kaper, *Catal. Today*, 2019, **333**, 105-112.
8. S. Gatla, D. Aubert, G. Agostini, O. Mathon, S. Pascarelli, T. Lunkenbein, M. G. Willinger and H. Kaper, *ACS Catal.*, 2016, **6**, 6151-6155.
9. J. Lee, Y. Ryou, J. Kim, X. Chan, T. J. Kim and D. H. Kim, *J. Phys. Chem. C*, 2018, **122**, 4972-4983.

5. References

1. K. Jiang, B. Y. Liu, M. Luo, S. C. Ning, M. Peng, Y. Zhao, Y. R. Lu, T. S. Chan, F. M. F. de Groot and Y. W. Tan, *Nat. Commun.*, 2019, **10**.
2. L. R. Merte, F. Behafarid, D. J. Miller, D. Friebel, S. Cho, F. Mbuga, D. Sokaras, R. Alonso-Mori, T. C. Weng, D. Nordlund, A. Nilsson and B. Roldan Cuenya, *ACS Catal.*, 2012, **2**, 2371-2376.
3. Y. Jang, K. H. Choi, D. Y. Chung, J. E. Lee, N. Jung and Y. E. Sung, *ChemSusChem*, 2017, **10**, 3063-3068.
4. D. Chen, Q. Tao, L. W. Liao, S. X. Liu, Y. X. Chen and S. Ye, *Electrocatalysis*, 2011, **2**, 207-219.
5. D. A. Shapiro, R. Celestre, B. Enders, J. Joseph, H. Krishnan, M. A. Marcus, K. Nowrouzi, H. Padmore, J. Park, A. Warwick and Y.-S. Yu, *Microsc. Microanal.*, 2018, **24**, 8-11.
6. H. L. Xin, K. Niu, D. H. Alsem and H. Zheng, *Microsc. Microanal.*, 2013, **19**, 1558-1568.
7. Y. A. Wu, L. Li, Z. Li, A. Kinaci, M. K. Y. Chan, Y. Sun, J. R. Guest, I. McNulty, T. Rajh and Y. Liu, *ACS Nano.*, 2016, **10**, 3738-3746.
8. E. Paparazzo, G. M. Ingo and N. Zacchetti, *J. Vac. Sci. Technol. A*, 1991, **9**, 1416-1420.
9. L. A. J. Garvie and P. R. Buseck, *J. Phys. Chem. Solids*, 1999, **60**, 1943-1947.
10. M. R. Howells, T. Beetz, H. N. Chapman, C. Cui, J. M. Holton, C. J. Jacobsen, J. Kirz, E. Lima, S. Marchesini, H. Miao, D. Sayre, D. A. Shapiro, J. C. H. Spence and D. Starodub, *J. Electron. Spectrosc.*, 2009, **170**, 4-12.
11. G. Kresse and J. Furthmuller, *Phys. Rev. B*, 1996, **54**, 11169-11186.
12. G. Kresse and D. Joubert, *Phys. Rev. B*, 1999, **59**, 1758-1775.
13. J. P. Perdew and Y. Wang, *Phys. Rev. B*, 1992, **45**, 13244-13249.
14. S. L. Dudarev, G. A. Botton, S. Y. Savrasov, C. J. Humphreys and A. P. Sutton, *Phys. Rev. B*, 1998, **57**, 1505-1509.
15. J. B. Park, J. Graciani, J. Evans, D. Stacchiola, S. G. Ma, P. Liu, A. Nambu, J. F. Sanz, J. Hrbek and J. A. Rodriguez, *Proc. Natl. Acad. Sci. U. S. A.*, 2009, **106**, 4975-4980.
16. H. Y. Kim, M. S. Hybertsen and P. Liu, *Nano Lett.*, 2017, **17**, 348-354.
17. P. E. Blochl, *Phys. Rev. B*, 1994, **50**, 17953-17979.
18. A. G. Thomas, W. R. Flavell, A. K. Mallick, A. R. Kumarasinghe, D. Tsoutsou, N. Khan,

C. Chatwin, S. Rayner, G. C. Smith, R. L. Stockbauer, S. Warren, T. K. Johal, S. Patel, D. Holland, A. Taleb and F. Wiame, *Phys. Rev. B*, 2007, **75**, 035105.

19. A. Henningsson, H. Rensmo, A. Sandell, H. Siegbahn, S. Södergren, H. Lindström and A. Hagfeldt, *J. Chem. Phys.*, 2003, **118**, 5607-5612.
20. A. C. Johnston-Peck, S. D. Senanayake, J. J. Plata, S. Kundu, W. Xu, L. Barrio, J. Graciani, J. F. Sanz, R. M. Navarro, J. L. G. Fierro, E. A. Stach and J. A. Rodriguez, *J. Phys. Chem. C*, 2013, **117**, 14463-14471.
21. C. L. Melcher, S. Friedrich, P. Cramer, M. A. Spurrier, P. Szupryczynski and R. Nutt, *IEEE Trans. Nucl. Sci.*, 2005, **52**, 1809-1812.
22. K. Ding, A. Gulec, A. M. Johnson, N. M. Schweitzer, G. D. Stucky, L. D. Marks and P. C. Stair, *Science*, 2015, **350**, 189-192.
23. L. DeRita, S. Dai, K. Lopez-Zepeda, N. Pham, G. W. Graham, X. Pan and P. Christopher, *J. Am. Chem. Soc.*, 2017, **139**, 14150-14165.
24. L. Nie, D. Mei, H. Xiong, B. Peng, Z. Ren, X. I. P. Hernandez, A. DeLaRiva, M. Wang, M. H. Engelhard, L. Kovarik, A. K. Datye and Y. Wang, *Science*, 2017, **358**, 1419-1423.